ACS APPLIED MATERIALS & INTERFACES

Research Article

Cite This: ACS Appl. Mater. Interfaces 2018, 10, 37316−37325

www.acsami.org

Brightness Enhancement in Pulsed-Operated Perovskite Light-Emitting Transistors

Francesco Maddalena,[†] Xin Yu Chin,[‡] Daniele Cortecchia,[‡,§] Annalisa Bruno,[‡] and Cesare Soci*[,†,∥]

[†]Division of Physics and Applied Physics, School of Physical and Mathematical Sciences, and [∥]Centre for Disruptive Photonic Technologies, TPI, Nanyang Technological University, 637371, Singapore

[‡]Energy Research Institute @ NTU, Nanyang Technological University, 637553, Singapore

[§]Interdisciplinary Graduate School, Nanyang Technological University, 639798, Singapore

Supporting Information

ABSTRACT: Perovskite light-emitting field-effect transistors (PeLEFETs) provide a versatile device architecture to control transport and electroluminescence properties of hybrid perovskites, enabling injection of high charge carrier density and spatial control of the radiative recombination zone. Ionic screening and organic cation polarization effects typical of metal-halide perovskites, however, critically affect PeLEFET efficiency and reliability. In this work, we demonstrate a new device operation mode based on high-frequency modulation of the applied voltages, which allows significant reduction of ionic drift/screening in methylammonium lead iodide light-emitting transistors. In optimized top contact PeLEFETs, AC operation results in brighter and more uniform electroluminescence compared to DC-driven devices, whereas high-frequency modulation enables electroluminescence emission up to room temperature.

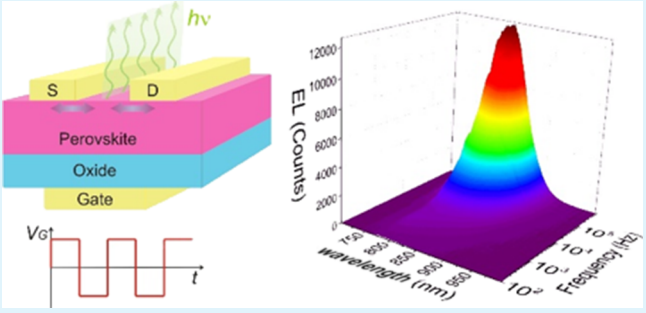

KEYWORDS: *metal-halide perovskites, methylammonium lead iodide, light-emitting field-effect transistors, AC-driven light-emitting devices, space-charge field-assisted injection*

1. INTRODUCTION

Solution-processable hybrid organic−inorganic halide perovskites (HOIPs) are a class of materials with remarkable features such as high photoluminescence efficiencies,[1,2] long carrier lifetimes and diffusion lengths,[3−5] high mobility compared to typical solution-processed materials,[5−7] low thresholds in optical pumped lasing,[1,8] tunability of the optical band gap from the visible region to the near infrared (NIR),[9−11] and white light emission.[12,13] HOIPs have shown extremely good performance in photovoltaic devices,[14−16] photodetectors,[17] X-ray scintillation detectors,[18] and light-emitting diodes (LEDs).[2,19,20] HOIPs are also promising semiconductors for field-effect transistors (FETs).[6,21−27] Recently, a new light-emitting device concept was demonstrated, the perovskite light-emitting field-effect transistor (PeLEFET),[6] which however could only be operated at low temperatures.[28]

LEFETs offer several advantages compared to conventional LEDs, such as very high charge carrier densities and controllable current flow, charge injection, and emission patterns, which can lead to higher electroluminescence efficiencies.[29] Moreover, LEFETs integrate electroluminescence and electrical switching into the same device, potentially simplifying the architecture of active matrix displays.[30] Unfortunately, unlike their organic counterparts, PeLEFETs are severely affected by the problems of ionic motion[31,32] and cation polarization disorder,[33−37] which hamper their operational stability, reliability, and reproducibility. Ionic transport is mainly due to the presence of ion vacancies in the perovskite, which allow ions to move within the crystalline lattice.[31] The most probable source of ionic drift in methylammonium lead iodide is the iodine anion,[31] but cations are also known to contribute.[38] The disorder introduced by organic cations is caused by cation dipole fluctuations,[26] which can be preferentially reoriented under an applied electric field, particularly at a low temperature when the ions are less mobile. These phenomena have been known to produce several of the undesirable effects of perovskite devices, such as electrical hysteresis in solar cells,[39−41] unreliable operation of LEDs, causing fast degradation during operation,[42,43] lowering of the *effective* charge carrier mobility (by orders of magnitude compared to theoretical predictions or Hall-effect measurements),[5,26,44] and quenching of field effects in transistors.[6]

In our previous work, we showed that lowering the temperature below T = 200 K can effectively suppress the ionic motion within methylammonium lead iodide

Received: July 3, 2018
Accepted: October 2, 2018
Published: October 2, 2018

DOI: 10.1021/acsami.8b11057
ACS Appl. Mater. Interfaces 2018, 10, 37316−37325

($CH_3NH_3PbI_3$) PeLEFETs.[6] Low temperature was necessary to reduce ion-induced gate screening and increase effective mobility, giving rise to gate-controlled charge injection and electroluminescence from the transistor channel. In this work, we present a new operational concept to overcome the detrimental effects of ionic drift and cation polarization in PeLEFETs, based on high-frequency AC modulation of the source/drain or gate bias. We show that the AC-driven PeLEFETs are characterized by brighter and more uniform electroluminescence than DC-driven PeLEFETs at comparable applied voltages.

Figure 1 shows different operational configurations of PeLEFETs used in this work. In DC-driven PeLEFETs[6]

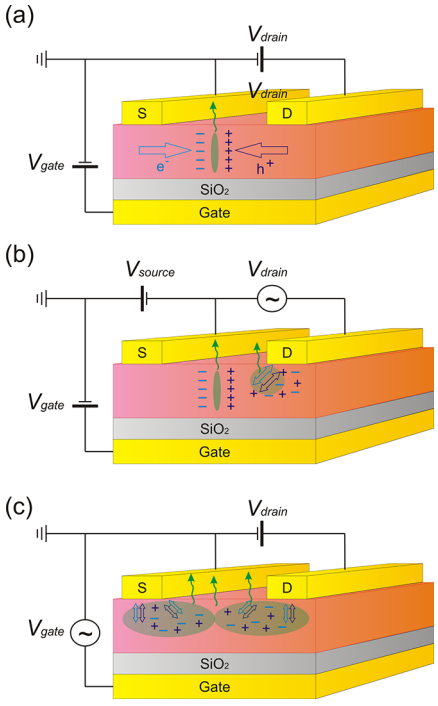

Figure 1. Schematics of PeLEFETs in different operation modes: (a) DC-driven PeLEFETs: holes and electrons are injected continuously from the source and the drain and recombine in a thin zone within the channel; (b) AC-driven drain PeLEFETs: in addition to continuously injected charges because of the applied source bias, both electrons and holes are injected consecutively from the drain; (c) AC-driven gate PeLEFETs: holes and electrons are injected consecutively from the source and the drain. Charge diffusion can be controlled by the lateral drain/source field.

(Figure 1a), electrons and holes are steadily injected from the source and drain and meet within the channel, giving rise to a thin recombination zone, which can be moved by tuning the drain and gate bias. However, the DC bias induced strong ionic migration and methylammonium cation (MA^+) polarization of the perovskite. In AC-driven drain PeLEFETs (Figure 1b), the drain is driven by an AC voltage, whereas a DC bias is applied to the gate and the source. Finally, in AC-driven gate PeLEFETs (Figure 1c) an AC bias is applied to the gate, whereas a DC bias is applied between the source and the drain. Application of ac-biases, especially at high frequencies, is expected to impede the ionic migration and the polarization of the methylammonium cation, if the driving frequency is faster than the response times of such phenomena, hence improving device efficiency.

In this work, we show that the AC-driven PeLEFET is characterized by brighter and more uniform electroluminescence than DC-driven PeLEFETs at comparable applied voltages. By tuning the drain bias and the amplitude of the gate bias, we also observe uniform emission from the whole transistor channel. Importantly, high-frequency AC operation enables electroluminescence emission at significantly higher temperatures, including room temperature. In addition, we observe that luminescence yield and efficiency of AC-driven PeLEFETs increase with applied frequency up to the megahertz range. This makes AC-driven PeLEFETs an excellent candidate not only for lighting and displays (with active perovskites emitting in the visible) but also for light communication technologies, such as visible light communication (VLC)[45] and infrared communication (IRC).

2. MATERIALS AND METHODS

2.1. Perovskite Synthesis and Deposition. Methylammonium lead iodide ($CH_3NH_3PbI_3$) thin films were prepared from 1 M precursor solutions of CH_3NH_3I (Dyesol) and PbI_2 (99.99%, TCI) (molar ratio 1:1) in anhydrous dimethylformamide (DMF). Prior to the deposition of the perovskite, the substrates (see section 2.3. FET Fabrication and Characterization) were cleaned with ultrasonication for 5 min in demineralized water, acetone, and isopropanol and successively dried with compressed air. An oxygen plasma cleaning treatment was performed on the substrates, for 90 s, to improve the wetting of the surface and obtain flatter and homogeneous perovskite thin films. The DMF solution was spin-coated onto the substrates with a speed of 5000 rpm for 30 s. Toluene was drop-casted on the substrates 4 s after the start of the spin-coating program. The resulting film was finally annealed at 100 °C for 15 min.

2.2. Atomic Force Spectroscopy and X-ray Diffraction. The scanning probe microscope Cypher ES, Asylum Research, was used for atomic force microscopy (AFM) measurements. The software Gwyddion was used for editing and plotting of the AFM images. The X-ray diffraction (XRD) diffractograms were obtained using a diffractometer Bruker D8 ADVANCE with Bragg−Brentano geometry employing Cu Kα radiation (λ = 1.54056 Å), step increment of 0.02°, and 1 s of acquisition time.

2.3. FET Fabrication and Characterization. Heavily p-doped Si substrates were used as the bottom gate electrode, with a 500 nm thick thermally grown silicon oxide layer as the gate insulator with a capacitance of 6.9 nF cm^{-2}. The perovskite was deposited as described above, and top contact gold source and drain electrodes (channel length: 100 μm, channel width: 1 mm) were deposited by thermal evaporation through a shadow mask on top of the previously deposited perovskite layer. The FETs were measured in vacuum (10^{-3} mbar) and dark at different temperatures ranging from 78 to 300 K using a liquid nitrogen-cooled Linkam stage (HFS600E-PB4/PB2) with an LNPT95 system controller. The transistor DC characteristics, with forward and reverse scans, were acquired with Agilent B2902A Precision Source/Measure Unit. The mobility of the electrons was determined using the conventional equations for metal-oxide-semiconductor (MOS) transistors in a saturated regime.[46] The AC-driven measurements were conducted applying a square wave bias on the PeLEFET gate electrode, using a Rigol DG5101 function/arbitrary waveform generator coupled with a Falco Systems WMA-300 high-voltage amplifier. Measurement of the current during the AC-driven tests was carried out as described in the Supporting Information (Figure S10).

2.4. Electroluminescence Characterization. Optical images and recordings were acquired using a PCO.edge 3.1 sCMOS camera coupled to an optical microscope. Spectra were collected using an Avantes AvaSpec ULS-RS-TEC. The time-dependent electroluminescent response of the PeLEFET with the applied bias was collected by using a Newport 818-UV photodiode connected to a Stanford Research Systems SR570—low-noise current preamplifier and a LeCroy WaveSurfer 104MXs-B oscilloscope. The applied bias to the

DOI: 10.1021/acsami.8b11057
ACS Appl. Mater. Interfaces 2018, 10, 37316−37325

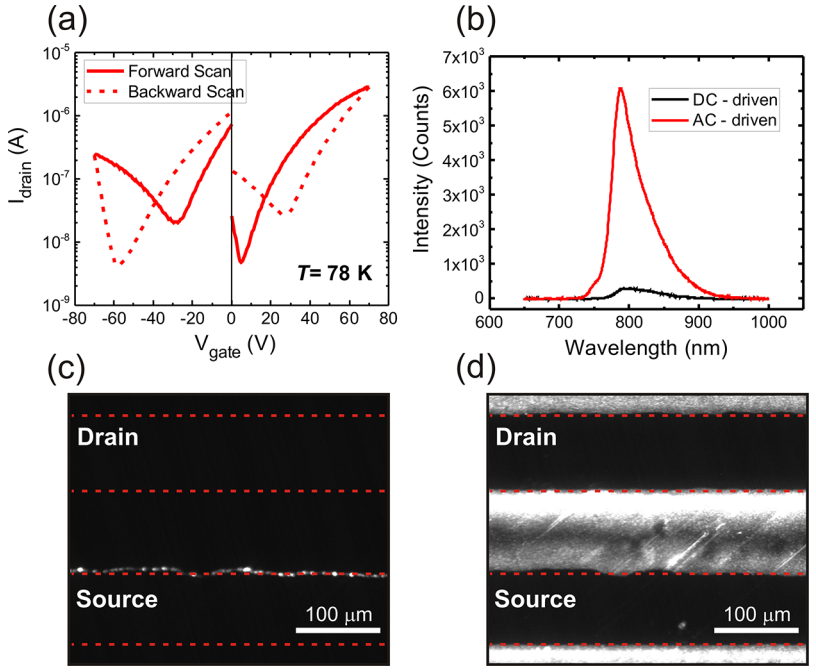

Figure 2. (a) Low-temperature transfer characteristics of the DC-driven PeLEFET. (b) Spectra of a PeLEFET driven in dc- and ac-modes at comparable voltages (dc: V_{drain} = 50 V, V_{gate} = 100 V; ac: V_{drain} = 50 V, V_{gate} = ±100 V, 10 kHz square wave), showing the difference in electroluminescence between the two driving modes. Channel of the top contact, bottom gate PeLEFET with electroluminescence at T = 78 K from (c) DC-driven PeLEFET (V_{drain} = 50 V, V_{gate} = 100 V), showing very low electroluminescence signal; (d) AC-driven PeLEFET with a 10 kHz square wave applied to the gate (V_{drain} = 50 V, V_{gate} = ±100 V).

PeLEFET and trigger for the oscillocope was obtained from the Rigol DG5101 function/arbitrary waveform generator connected to the Falco Systems WMA-300 high-voltage amplifier. The efficiency of the PeLEFET was calculated using a Thorlabs LED851W infrared LED as described in the Supporting Information (Figure S14).

3. RESULTS AND DISCUSSION

We fabricated PeLEFETs in the top contact, bottom gate configuration, as shown in Figure 1. The morphology of HOIPs is very sensitive to the deposition method; hence, charge transport and electroluminescence characteristics are also closely tied to how the perovskite is deposited onto the substrate.[47] In this work, we used a modified version of the "solvent engineering" method[48] to achieve a compact, smooth, crystalline, and uniform $CH_3NH_3PbI_3$ film, obtaining good contact between the perovskite and the top contact source and drain electrodes and improving the charge carrier mobility compared to our previous work.[6] The resulting films are compact polycrystalline films with ∼200 nm domains with a relatively smooth surface (R_{rms} = 6.79 nm), as seen from the AFM profile shown in Figure S1b. $CH_3NH_3PbI_3$ crystallizes the characteristic room-temperature tetragonal phase with high purity and virtually absent unreacted PbI_2, as revealed by the XRD analysis in Figure S1b.

Lowering the operating temperature below T = 200 K decreases the ionic motion within the perovskite, significantly reducing its negative effects on device operation, hence recovering transistor-like behavior.[6,26] Figure 2a shows the transfer curves of the top contact PeLEFET at T = 78 K. The PeLEFET has clear ambipolar behavior, which allows controlled injection of both charge carriers, hence tuning the position of the radiative recombination zone within the transistor channel,[6,49,50] as shown in Figure S2.

Depending on the drain and gate biases applied, charge recombination and light emission occur either close to the drain or source electrode or within the transistor channel itself. Hysteresis in the current−voltage characteristics is still present even at low temperatures, and can be attributed not only to remnant ionic motion, but also to the presence of traps in the material.[26,51,52] Thanks to the improved morphology and charge injection by top contact configuration,[53] mobilities of 0.11 $cm^2\ V^{-1}\ s^{-1}$ for electrons and 0.025 $cm^2\ V^{-1}\ s^{-1}$ for holes were achieved at T = 78 K, which are higher than those previously reported for $CH_3NH_3PbI_3$ devices with the same precursors and stoichiometry, yet significantly lower than theoretically predicted values.[5,6,26] For both electrons and holes, the mobility decreases slightly at higher temperatures, up until T = 178 K, when it starts to decrease exponentially (Figure S3). This is consistent with previous theoretical and experimental observations of the dependence of charge carrier mobility on the transition from the orthogonal to the tetragonal phase in methylammonium lead iodide;[6,7,26] when the perovskite is in the tetragonal phase, the polarization of the methylammonium cations causes energetic disorder at low temperatures (below ∼250 K), hindering charge transport, whereas at higher temperatures the effect of ionic motion becomes the dominant factor affecting charge carrier mobility.[26]

Another approach to mitigate the negative effects of ionic drift and methylammonium cation polarization on charge transport and electroluminescence is the AC-driven PeLEFET. Figure 2c,d shows the comparison between the PeLEFET driven in DC mode and AC-driven gate mode at comparable voltages. The AC-driven PeLEFET exhibits higher electroluminescence than the DC-driven PeLEFET. When operated in dc-mode (Figure 2c), at V_{drain} = 50 V and V_{gate} = 100 V, the PeLEFET electroluminescence is barely visible and radiative

DOI: 10.1021/acsami.8b11057
ACS Appl. Mater. Interfaces 2018, 10, 37316−37325

recombination occurs only in a few spots, forming a narrow emission line close to the source electrode. On the other hand, when the PeLEFET gate is driven in AC mode (Figure 2d) with comparable voltages, V_{drain} = 50 V and V_{gate} = ±100 V by a 10 kHz square wave, the observed electroluminescence is strikingly higher, and light is emitted both from the edges of the drain and the source electrodes, and within the transistor channel. Figure 2b shows the emission spectra of the PeLEFET device driven in DC and AC modes with voltages used in Figure 2c,d. The maximum of the electroluminescence spectrum in ac-mode (at 10 kHz) is 20 times higher than in dc-mode. The increment in electroluminescence can be attributed to the reduction of ionic drift and MA^+ polarization as well as to improved carrier injection. DC bias causes the drift of iodine ion vacancies and respective ions, which eventually accumulate on one side of the device. This induces an electric field that screens the gating field, thus impeding charge transport and radiative recombination. On the other hand, if an ac-bias, such as a symmetric square wave, is applied to the gate, the movement of ion vacancies is restricted to an oscillation about the original point of origin, preventing accumulation of vacancies on one single side of the device. The same principle applies to lead and methylammonium ionic vacancies. Moreover, driving the bias at sufficiently high frequencies is also expected to avoid the effects of distortions induced by MA^+ polarization, if the period of the applied bias wave is faster than the MA^+ cation induced distortion reorientation time. Although the rotation speed of the methylammonium cation under an applied bias was determined to be as fast as a few picoseconds, the relaxation timescale of distortion domains caused by the MA^+ reorientation in methylammonium lead iodide was estimated to be around 0.1−1 ms,[54] which is within the range of operation of the AC-driven PeLEFET described in this work.

The electroluminescence observed in the AC-driven PeLEFET (Figure 2c,d) appears to originate not only within the channel of the transistor, but also from beneath the PeLEFET drain and source electrodes. This phenomenon has been previously observed in organic AC-driven LEFETs,[55−63] and was attributed to *AC field-induced electroluminescence* (AIFEL).[55−57] The operation of the FET is fundamentally based on the principles of the metal−insulator−semiconductor (MIS) diode.[46] In our devices, both gate/source and gate/drain electrode pairs can be viewed as two separate MIS diodes where one electrode is in contact with the semiconductor and acts as the injecting electrode (either the source or the drain electrode), whereas the other electrode, separated by an insulating layer, acts as the gate. When a bias is applied between the gate and the injecting electrode, holes or electrons are sequentially injected around the electrodes. This phenomenon was also observed in purely capacitive electroluminescent devices with organic semiconductor active materials.[57,64−66] The electroluminescence of the AC-driven PeLEFET increases with amplitude of the applied gate bias, as seen in Figure S4. The dependence of the electroluminescence with the gate voltage is superlinear, becoming quadratic at driving frequencies higher than 10 kHz. A quadratic relationship has been previously reported for AC-driven LEFETs with organic semiconductor emitters.[63,67]

The spatial position of the carrier recombination (light emission) zone of the AC-driven PeLEFET can be controlled by modifying the gate or source drain voltages of the device, similarly to its DC-driven counterpart. This can be achieved in both cases of AC-driven drain or gate electrodes. As shown in Figure 3a, by applying an alternating bias (±50 V, 10 kHz) to the drain electrode and keeping the gate bias constant (+20 V), the emission zone of the PeLEFET moves through the channel while sweeping the source bias. By varying the source bias from +30 to +80 V, the recombination zone moves from the source (Figure 3a, top panel) to the middle of the channel (Figure 3a, middle panel), to the drain electrode (Figure 3a, bottom panel). It is important to note that, because of the AC bias applied to the drain electrode, there is *always* an emission contribution because of the AIFEL effect between the drain and the gate. The position of the recombination zone can also be tuned by applying a square wave to the gate and sweeping the drain bias. This is shown in Figure S5, where V_{gate} = ±50 V (square wave, 10 kHz) and the drain bias is swept from 20 to 80 V. Here, the AIFEL effect clearly results in electroluminescence emission from the edges of the drain and source electrodes. In addition to having a spatially tunable recombination zone, tuning the gate and drain bias of the AC-driven gate PeLEFET allows achieving bright emission from the entire transistor channel (Figure 3b). By applying a small (positive) bias to the drain electrode (V_{source} = +10 V), electroluminescence is observed mainly from the edges of the source and drain electrodes (Figure 3b, top panel). By making the drain bias steadily more negative, the recombination zone moves within the transistor channel (Figure 3b, middle panel) and, if the drain bias is sufficiently negative, light is emitted uniformly from the whole channel (Figure 3b, bottom panel). Hence, by applying an AC bias to the gate electrode, the source/drain and the gate electrodes can be capacitively coupled; the lateral field between the source and the drain electrodes induces charge carriers to drift and recombine

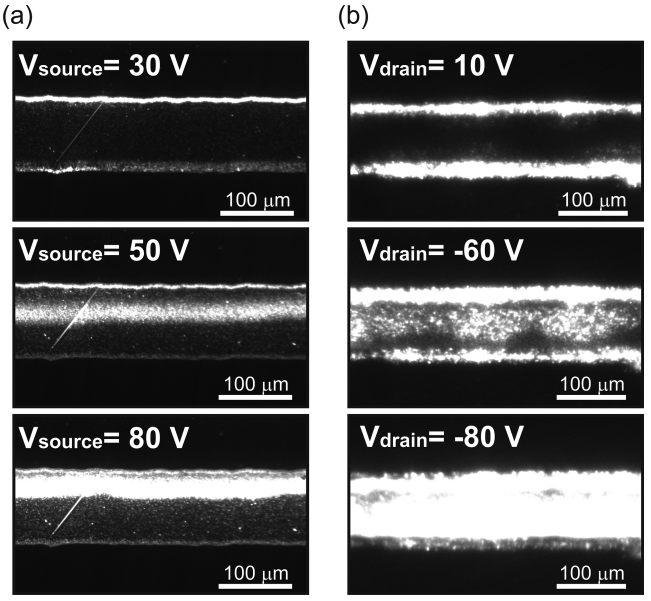

Figure 3. Low-temperature (T = 78 K) electroluminescence from the AC-driven PeLEFET in different operating conditions. (a) AC-driven drain: V_{drain} = ±50 V (10 kHz square wave), V_{gate} = 20 V and, from top to bottom, V_{source} = 30 V, V_{source} = 50 V, and V_{source} = 80 V, respectively. (b) AC-driven gate: V_{gate} = ±60 V (10 kHz square wave) and, from top to bottom, V_{drain} = 10 V, V_{drain} = −60 V, and V_{drain} = −80 V, respectively.

DOI: 10.1021/acsami.8b11057
ACS Appl. Mater. Interfaces 2018, 10, 37316−37325

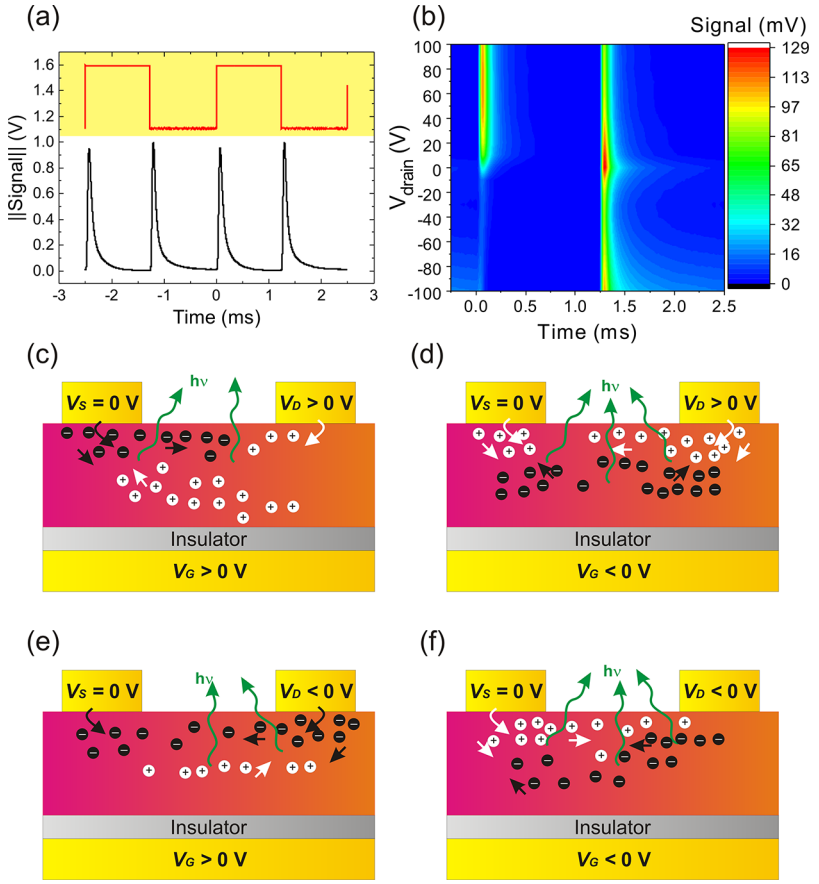

Figure 4. (a) Normalized plots of the applied square wave bias (top) and intensity of the electroluminescence signal response at 400 Hz, V_{drain} = 30 V, V_{gate} = ±50 V, and T = 78 K (bottom). (b) Contour plot of the electroluminescence response of the AC-driven gate PeLEFET at 400 Hz, V_{gate} = ±50 V, and T = 78 K, for different drain biases. The polarity of the applied square wave was +50 V at $0 \leq t \leq 1.25$ ms and −50 V at $1.25 \leq t \leq 2.5$ ms. (c–f) Schematics of the operation of the AC-driven gate PeLEFET for positive drain bias and positive (c) or negative (d) gate bias, and for negative drain bias and positive (e) or negative (f) gate polarization.

throughout the channel, overall resulting in a wide and uniform emission zone across the top contacts.

The time evolution of the electroluminescence response of the PeLEFET to the square wave applied to the gate is shown in Figure 4a,b. For sufficiently low frequencies, distinct electroluminescence peaks can be observed in response to positive and negative amplitudes of the square wave, as shown in Figures 4a and S6 for a driving frequency of 400 Hz. The height of the electroluminescence peaks for positive and negative amplitudes varies according to the applied biases. By keeping the amplitude of the square wave constant, while varying the applied drain bias, the height and decay times of the peaks change significantly (Figure 4b). For positive drain bias, electroluminescence occurs for both positive and negative polarities of the square wave applied to the gate, whereas for the negative drain bias light is emitted only during the half-cycle with negative polarity. As the drain bias becomes more positive, the electroluminescence intensity in the half-cycle with positive polarity of the square wave increases, whereas in the half-cycle with negative polarity it is slightly reduced. In the case of negative drain bias, the electroluminescence peak in the half-cycle with positive polarity is increasingly suppressed as the drain bias becomes more negative, whereas in the half-cycle with negative polarity it weakens up to $V_{drain} \approx -30$ V, below which it becomes prominent and takes longer to decay, to the point where the decay time exceeds the period of the applied wave. This is consistent with uniform light emission observed throughout the channel at large negative drain bias amplitudes (Figure 3b).

The electroluminescence peaks can be phenomenologically modeled using an asymmetric double sigmoidal function (Figure S7) to describe the rise and decay times (Figure S8). The rise times of the peaks show little dependence on the applied drain bias, ranging between 9.6 and 11.3 μs when the square wave has a positive amplitude, and between 8.4 and 9.5 μs when the square wave has a negative amplitude. The rise time of the signal is likely due to electroluminescence deriving from the AIFEL effect, where charges that are injected at the beginning of a half-cycle of the square wave could recombine with charge carriers of the opposite sign accumulated in the preceding half-cycle. Here, charge carriers need only to travel distances of ∼100 nm between the source/drain electrodes and the gate. The transit time can then be approximated by $\tau \approx \frac{L}{\mu E} = \frac{L^2}{\mu V_{eff}}$, where L is the distance crossed, μ the charge carrier mobility, and V_{eff} the effective voltage potential experienced by the charge carriers,[61] which is of the order of 15 ps for electrons and 67 ps for holes. The longer electroluminescence rise time observed in our experiments may arise from capacitive limitations, as the RC cut-off time of the drain/source-perovskite-oxide−gate MOS-capacitor is estimated to be around ∼0.2 μs, corresponding to a cut-off frequency of 500 kHz, when the perovskite is in a low resistivity state.[68] The decay of the electroluminescence signal

DOI: 10.1021/acsami.8b11057
ACS Appl. Mater. Interfaces 2018, 10, 37316−37325

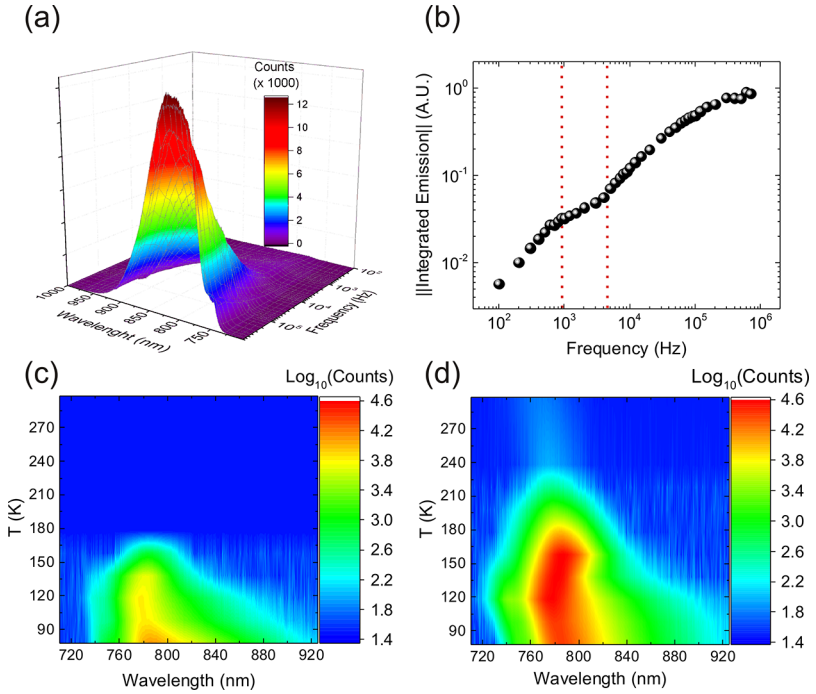

Figure 5. (a) Low-temperature (T = 78 K) electroluminescence emission spectra of the PeLEFET with AC-driven gate (square wave) at different frequencies (from 100 to 700 kHz), V_{drain} = −40 V and V_{gate} = ±60 V. (b) Normalized integrated emission of the electroluminescence peaks vs driving voltage frequency. The black dots are derived from the spectra at V_{drain} = −40 V and V_{gate} = ±60 V (T = 78 K). (c) Contour plot of the temperature-dependent emission spectra of the DC-driven PeLEFET (V_{drain} = 150 V, V_{gate} = 100 V). (d) Contour plot of the temperature-dependent emission spectra of the AC-driven PeLEFET (V_{drain} = −80 V, V_{gate} = ±60 V, 100 kHz modulation frequency).

can be fitted with no less than to different decay times. The shorter decay time lies between ∼35 and 45 μs, whereas the longer time lies between ∼150 and 250 μs. The average ratio between the longer and shorter decay times is ∼5, which is comparable to the ratio of the measured hole and electron mobilities as T = 78 K. This seems to indicate that the decay times are correlated to the mobility of charge carriers, with the shorter time relating to the transit time of electrons and the longer time relating to the transit time of holes. As the decay times do not vary significantly with applied drain voltage, the effective voltage V_{eff} in the relation above appears to be almost independent of drain bias. This suggests that charge carriers involved in the recombination events experience screened gate and drain/source potentials.

From the above observations, we propose a physical description of the operation of the AC-driven gate PeLEFET for the different bias conditions, which is summarized in Figure 4c–f. In all cases, light emission is expected from the edges of and under the electrodes because of the AIFEL effect, given that charge carriers injected by the source and drain electrodes have a high chance to meet and recombine with opposite charge carriers accumulated under or in the very close proximity of the injecting electrodes during the preceding half-cycle. With positive drain bias (Figure 4c,d), electrons would tend to move toward the drain and holes toward the source. For positive AC gate bias polarity (Figure 4c), electrons are injected from the source and drift toward both the gate and the drain, whereas holes are injected from the drain and drift mainly toward the source. Holes injected from the drain would also drift toward the source. Holes already present in the perovskite are driven toward the injecting electrodes, mainly the source, whereas electrons drift toward the gate dielectric and accumulate at the interface. Hence, radiative recombination is observed primarily from the vicinity of the source electrode, but also in regions of the channel where electrons and holes meet. When the bias polarity is reversed (Figure 4d), holes are injected from the source and the drain, accumulating close to the source and drifting mainly toward the gate dielectric. Holes already present in the perovskite are driven toward the gate dielectric and electrons toward the injecting electrodes, particularly toward the drain. Also, in this case, light emission is expected to occur mainly near the electrodes, where electrons meet newly injected holes, but also from within the channel. This picture is consistent with the bright electroluminescence observed in the proximity of the electrodes for positive drain biases (except at very high fields), and with the existence of an additional recombination zone that can be moved within the channel, as shown in Figure 3b (top panel) and Figure S5. Moreover, this is also in agreement with time-resolved measurements, where a large electroluminescence peak intensity was recorded for both positive and negative gate polarities. The relative peak amplitude at positive and negative gate polarities indicates that, at a positive gate bias, electroluminescence increases for increasing positive drain bias (Figure S6). This can be attributed to the fact that holes are the slowest charge carriers, and thus take longer to drift back to the injecting electrodes once the gate polarity is reversed, hence resulting in a higher concentration of holes than electrons at a large positive bias. Overall, this increases the recombination yield when holes drift away from the gate–insulator interface, that is in the positive gate polarity half-cycle. With negative drain bias (Figure 4e,f), electrons would tend to move toward the source and holes toward the drain electrodes. For positive AC gate bias polarity (Figure 4e), electrons injected from the source would drift toward the gate dielectric, whereas electrons injected from the

DOI: 10.1021/acsami.8b11057
ACS Appl. Mater. Interfaces 2018, 10, 37316–37325

Table 1. Integrated Electroluminescence, Luminosity, I_{rms}, V_{rms}, Device Area, Power, and Efficiency of the PeLEFET Driven in DC Mode (V_D = 100 V, V_G = 100 V) and AC Mode (V_D = 100 V, V_G = ±100 V) for Different Frequencies at T = 78 K and a Reference Commercial NIR LED

device	integrated EL [counts]	luminosity [cd m^{-2}]	I_{rms} [A]	power [W m^{-2}]	efficiency [lm W^{-1}]
DC-driven	4.90×10^{3}	4.60×10^{-3}	6.28×10^{-6}	6.28×10^{3}	$2.30 \pm 0.11 \times 10^{-6}$
F = 1 kHz	1.17×10^{4}	1.10×10^{-2}	1.21×10^{-5}	1.21×10^{4}	$2.86 \pm 0.12 \times 10^{-6}$
F = 10 kHz	1.83×10^{5}	1.72×10^{-1}	7.94×10^{-5}	7.94×10^{4}	$6.81 \pm 0.29 \times 10^{-6}$
F = 100 kHz	9.99×10^{5}	9.38×10^{-1}	3.54×10^{-4}	3.54×10^{5}	$8.33 \pm 0.35 \times 10^{-6}$

drain would drift toward the gate dielectric and the source. Radiative recombination could then occur with carriers injected from the previous half-cycle drifting toward the electrodes, especially the drain. The electroluminescence peak during the positive polarization of the gate is very weak and decreases for increasingly negative drain bias. This indicates that relatively few holes accumulate in this regime, consistent with their lower mobility and hence longer transit time compared to the electrons. For negative polarity of the AC gate bias (Figure 4f), holes are injected from the source and drift toward the drain, whereas electrons injected from the drain move toward the source. In this case, the device is electron-dominated and light emission is determined by holes injected from the source and recombining with electrons already present in the perovskite. From Figure 3b (middle and bottom panels), at a negative drain bias recombination seems to occur both near the electrodes and within the channel, indicating that holes effectively drift within the channel and recombine with electrons throughout. Moreover, for a negative gate bias, the electroluminescence peak is much more intense and is long-lived, according to the hole transit time in the device.

The electroluminescence spectra of the PeLEFET driven at different frequencies, from 100 to 700 kHz, are shown in Figure 5a. The corresponding frequency dependence of the integrated electroluminescence signal is shown in Figure 5b. At low frequencies, up to ∼1 kHz, the electroluminescence intensity is linearly dependent on frequency, and the decay time of the electroluminescence pulses is smaller than the half-period of the applied square wave (Figure 4a). In this regime, the integrated emission intensity is simply proportional to the number of pulses per unit time (modulation frequency). As the electroluminescence pulses get closely spaced, relative to the intrinsic decay time of the pulses, the integrated electroluminescence signal saturates and eventually declines when the period of the AC bias wave is faster than the pulse rise time (corresponding to frequencies of 10−20 kHz). Overall, the electroluminescence signal never saturates or declines between 4 and ∼500 kHz modulation frequency. This follows a similar trend to the rise of the dielectric loss in response to the frequency for perovskites at a low temperature,[26] which is possibly caused by the polarization of the MA^+ cations within the perovskite.[26,37,69−71] The transition range observed between 1 and 10 kHz in Figure 5b is consistent with the characteristic relaxation times of 0.1−1 ms[54] of distortions induced by the polarization of MA^+. Hence, by increasing the modulation frequency, the polarization of MA^+ cations is expected to reduce and have less impact on transport and light emission characteristics of the device.

This is corroborated by the observed increase in electroluminescence and the increase in the root mean square (rms) current measured in AC-driven devices. As shown in Table 1, the rms current increases sublinearly in the device with increasing applied bias frequency and is higher than the current measured in DC-driven devices at comparable voltages. The increased current partially explains the higher electroluminescence compared to the DC-driven PeLEFET (Figure 2b−d) and the increase of electroluminescence with gate frequency (Figure 5a,b). The increase in the current is attributed to improved injection because of *space-charge field-assisted* charge injection.[63] When the gate is driven with AC bias, both charge carrier types are sequentially injected from the same electrode rather than one type of charge carrier being continuously injected (either from the source or the drain). In this situation, during a half-period of the gate bias (square) wave, one charge carrier type is injected and accumulates within the perovskite, inducing a space-charge field near the electrode. When the gate bias is quickly reversed, at the start of the next half-period of the gate bias wave, the space-charge field caused by the accumulated charge carriers aids the injection of the charge carriers of the opposite sign by decreasing the injection barrier.[63] Notably, the current peaks at the reversal of the applied square wave bias are about 2 orders of magnitude higher than the DC current at the same drain and gate bias amplitudes and shorter than the corresponding electroluminescent signal (Figure S10). This leads to a strong emission from the edges of the electrodes (see Figures 3 and S5), where a large density of injected charge carriers recombines with accumulated carriers of the opposite sign (Figure 4c−f). Note that, in this biasing configuration, the transient current peaks (Figure S10) do not correlate directly with the electroluminescence peak intensity, indicating that electroluminescence is limited by charge accumulation in the channel and not by the injection of individual charge carriers through the contacts.

At modulation frequencies higher than ∼500 kHz, the rise time of the electroluminescence pulse saturates (up to ∼1.5 MHz) and successively declines (Figure S9). Above 4.5 MHz, no electroluminescence signal could be recorded. We attribute the saturation and decline of the electroluminescence signal to the cut-off frequency of the RC equivalent circuit, which is estimated to be around 500 kHz. In this high-frequency regime, accumulation of charge carriers during each half-cycle reduces, resulting in saturation and eventual reduction of electroluminescence, up to the point where charge carriers cannot be effectively accumulated in the PeLEFET. Furthermore, the spectrum of the PeLEFET shows a slight dependence on modulation frequency, probably because of the modulation of self-absorption in methylammonium lead iodide for varying depths of the recombination zone.

The reduction of ionic drift and MA^+ polarization in the AC-driven PeLEFET significantly improves the electroluminescent characteristics of the device even at higher temperatures. As shown in Figure 5c and reported previously,[6] electroluminescence of DC-driven PeLEFETs becomes negligible above 180−200 K. The sudden decrease in electroluminescence efficiency at high temperatures was mainly attributed to

DOI: 10.1021/acsami.8b11057
ACS Appl. Mater. Interfaces 2018, 10, 37316−37325

methylammonium cation polarization disorder, which becomes a significant source of energetic disorder in the tetragonal phase,[26] above ∼160 K. This is corroborated by the fast decay of the electroluminescence peaks measured at low frequencies (400 Hz) above 160 K (Figure S11), whereas at very high frequencies, such as 100 kHz, light emission is still significantly strong up to $T \approx 240$ K. At high frequencies, a clear electroluminescence signal can be observed up to room temperature (Figure 5d). The individual, normalized, spectra of the electroluminescence of the dc- and AC-driven PeLEFET at different temperatures are reported in Figure S12. As seen in Figure S13, the temperature dependence of the integrated electroluminescence signal is similar to that of the fluorescence signal of $CH_3NH_3PbI_3$, especially at temperatures higher than 160 K. This suggests that emission from the AC-driven PeLEFET is closely related to the intrinsic properties of the pristine active material in the absence of electric field-induced perturbations, such as ionic drift or MA^+ polarization. As expected, the total electroluminescence signal of the DC-driven PeLEFET seems to decay very quickly, similarly to the low-frequency (400 Hz) electroluminescence pulses (Figure S11), proving that high-frequency modulation of the PeLEFET effectively improves its performance at all temperatures, enabling room-temperature operation for the first time. The estimated electroluminescence efficiencies of the PeLEFET in DC and AC modes at low temperature ($T = 78$ K) are shown in Table 1. The overall efficiency is higher for AC-driven devices (Freq. >1 kHz) compared to the DC-driven PeLEFET. In addition, the efficiency increases with frequency, reaching the highest value of 8.33×10^{-6} lm W^{-1} at 100 kHz ($V_D = 100$ V, $V_G = \pm 100$ V). This indicates that the electroluminescence improvement is not only due to higher current densities achieved in the AC regime, but also the reduction of ionic migration and cation polarization effects, making the ac-PeLEFET intrinsically more efficient. Although the absolute efficiency of our PeLEFETs is relatively low compared to state-of-the-art perovskite LEDs, the device architecture and operation lends itself perfectly to light communication applications (e.g., VLC and IRC). In particular, the luminosity of PeLEFETs increases over a factor 100 from DC to AC operation at 100 kHz, together with the power efficiency, which may be promising for VLC and IRC at high bitrates.

4. CONCLUSIONS

In summary, we demonstrated AC-driven, top-contact methylammonium lead iodide PeLEFETs with controllable emission pattern and enhanced electroluminescence yield and efficiency compared to DC-driven devices. The improved electroluminescence is attributed to minimization of ionic vacancy drift and methylammonium cation polarization within the perovskite active layer as well as improved charge carrier injection because of space-charge field-assisted injection. By tuning the drain voltage and the amplitude of the gate bias, we could achieve uniform emission from the entire PeLEFET channel. Moreover, high-frequency AC operation enables electroluminescence emission at significantly higher temperatures than DC-driven PeLEFETs, approaching room temperature. We envision that further materials and device optimization, such as using high-k dielectrics,[72] asymmetric contacts[73] and device size scale-down, may lead to applications of PeLEFETs in ambient lighting, active matrix displays, and light communication technologies.

ASSOCIATED CONTENT

Supporting Information

The Supporting Information is available free of charge on the ACS Publications website at DOI: 10.1021/acsami.8b11057.

AFM and XRD measurements of methylammonium lead iodide; light emission from the DC-driven PeLEFET; temperature dependence of the charge carrier mobility of the DC-driven PeLEFET; gate dependence on the electroluminescence of the AC-driven PeLEFET; electroluminescence of the PeLEFET with AC-driven gate; EL response of the PeLEFET with the AC-driven gate at different drain biases; fitting of the time-resolved EL response of the PeLEFET to an applied square wave bias; rise and decay times of the EL peaks of the AC-driven gate PeLEFET; decay of the EL signal at high frequencies; time-resolved electroluminescence and current in an AC-driven PeLEFET; contour plot of time-resolved EL signal of the PeLEFET at different temperatures; temperature dependence of the electroluminescence spectra; plot of the normalized total electroluminescence for the ac- and DC-driven PeLEFET and the fluorescent signal of the perovskite from 78 to 298 K; and emission of the NIR-LED and calibration line (PDF)

AUTHOR INFORMATION

Corresponding Author

*E-mail: csoci@ntu.edu.sg.

ORCID

Cesare Soci: 0000-0002-0149-9128

Notes

The authors declare no competing financial interest.

ACKNOWLEDGMENTS

The research was supported by the Singapore Ministry of Education (grant nos. MOE2016-T1-1-164 and MOE2011-T3-1-005) and the Singapore National Research Foundation (CRP award no. NRF-CRP14-2014-03).

REFERENCES

(1) Deschler, F.; Price, M.; Pathak, S.; Klintberg, L. E.; Jarausch, D.-D.; Higler, R.; Hüttner, S.; Leijtens, T.; Stranks, S. D.; Snaith, H. J.; Atatüre, M.; Phillips, R. T.; Friend, R. H. High Photoluminescence Efficiency and Optically Pumped Lasing in Solution-Processed Mixed Halide Perovskite Semiconductors. *J. Phys. Chem. Lett.* **2014**, *5*, 1421−1426.

(2) Tan, Z.-K.; Moghaddam, R. S.; Lai, M. L.; Docampo, P.; Higler, R.; Deschler, F.; Price, M.; Sadhanala, A.; Pazos, L. M.; Credgington, D.; Hanusch, F.; Bein, T.; Snaith, H. J.; Friend, R. H. Bright Light-Emitting Diodes Based on Organometal Halide Perovskite. *Nat. Nanotechnol.* **2014**, *9*, 687−692.

(3) Stranks, S. D.; Eperon, G. E.; Grancini, G.; Menelaou, C.; Alcocer, M. J. P.; Leijtens, T.; Herz, L. M.; Petrozza, A.; Snaith, H. J. Electron-Hole Diffusion Lengths Exceeding 1 Micrometer in an Organometal Trihalide Perovskite Absorber. *Science* **2013**, *342*, 341−344.

(4) Chen, Y.; Yi, H. T.; Wu, X.; Haroldson, R.; Gartstein, Y. N.; Rodionov, Y. I.; Tikhonov, K. S.; Zakhidov, A.; Zhu, X.-Y.; Podzorov, V. Extended Carrier Lifetimes and Diffusion in Hybrid Perovskites Revealed by Hall Effect and Photoconductivity Measurements. *Nat. Commun.* **2016**, *7*, 12253.

(5) Maddalena, F.; Boix, P. P.; Chin, X. Y.; Mathews, N.; Soci, C.; Mhaisalkar, S. Charge Transport in Organometal Halide Perovskites.

DOI: 10.1021/acsami.8b11057
ACS Appl. Mater. Interfaces 2018, 10, 37316−37325

In *Organic–Inorganic Halide Perovskite Photovoltaics: From Fundamentals to Device Architectures*; Park, N.-G., Gratzel, M., Miyasaka, T., Eds.; Springer International Publishing, 2016; pp 201–222.
(6) Chin, X. Y.; Cortecchia, D.; Yin, J.; Bruno, A.; Soci, C. Lead Iodide Perovskite Light-Emitting Field-Effect Transistor. *Nat. Commun.* **2015**, *6*, 7383.
(7) Motta, C.; El-Mellouhi, F.; Sanvito, S. Charge Carrier Mobility in Hybrid Halide Perovskites. *Sci. Rep.* **2015**, *5*, 12746.
(8) Xing, G.; Mathews, N.; Lim, S. S.; Yantara, N.; Liu, X.; Sabba, D.; Grätzel, M.; Mhaisalkar, S.; Sum, T. C. Low-Temperature Solution-Processed Wavelength-Tunable Perovskites for Lasing. *Nat. Mater.* **2014**, *13*, 476–480.
(9) Heo, J. H.; Im, S. H.; Noh, J. H.; Mandal, T. N.; Lim, C.-S.; Chang, J. A.; Lee, Y. H.; Kim, H.-j.; Sarkar, A.; Nazeeruddin, M. K.; Grätzel, M.; Seok, S. I. Efficient Inorganic-Organic Hybrid Heterojunction Solar Cells Containing Perovskite Compound and Polymeric Hole Conductors. *Nat. Photon.* **2013**, *7*, 486–491.
(10) Stoumpos, C. C.; Malliakas, C. D.; Kanatzidis, M. G. Semiconducting Tin and Lead Iodide Perovskites with Organic Cations: Phase Transitions, High Mobilities, and Near-Infrared Photoluminescent Properties. *Inorg. Chem.* **2013**, *52*, 9019–9038.
(11) Noh, J. H.; Im, S. H.; Heo, J. H.; Mandal, T. N.; Seok, S. I. Chemical Management for Colorful, Efficient, and Stable Inorganic-Organic Hybrid Nanostructured Solar Cells. *Nano Lett.* **2013**, *13*, 1764–1769.
(12) Cortecchia, D.; Yin, J.; Bruno, A.; Lo, S.-Z. A.; Gurzadyan, G. G.; Mhaisalkar, S.; Brédas, J.-L.; Soci, C. Polaron Self-Localization in White-Light Emitting Hybrid Perovskites. *J. Mater. Chem. C* **2017**, *5*, 2771–2780.
(13) Dohner, E. R.; Jaffe, A.; Bradshaw, L. R.; Karunadasa, H. I. Intrinsic White-Light Emission from Layered Hybrid Perovskites. *J. Am. Chem. Soc.* **2014**, *136*, 13154–13157.
(14) Kojima, A.; Teshima, K.; Shirai, Y.; Miyasaka, T. Organometal Halide Perovskites as Visible-Light Sensitizers for Photovoltaic Cells. *J. Am. Chem. Soc.* **2009**, *131*, 6050–6051.
(15) Green, M. A.; Ho-Baillie, A.; Snaith, H. J. The Emergence of Perovskite Solar Cells. *Nat. Photon.* **2014**, *8*, 506–514.
(16) Saliba, M.; Matsui, T.; Seo, J.-Y.; Domanski, K.; Correa-Baena, J.-P.; Nazeeruddin, M. K.; Zakeeruddin, S. M.; Tress, W.; Abate, A.; Hagfeldt, A.; Grätzel, M. Cesium-Containing Triple Cation Perovskite Solar Cells: Improved Stability, Reproducibility and High Efficiency. *Energy Environ. Sci.* **2016**, *9*, 1989–1997.
(17) Ahmad, S.; Kanaujia, P. K.; Beeson, H. J.; Abate, A.; Deschler, F.; Credgington, D.; Steiner, U.; Prakash, G. V.; Baumberg, J. J. Strong Photocurrent from Two-Dimensional Excitons in Solution-Processed Stacked Perovskite Semiconductor Sheets. *ACS Appl. Mater. Interfaces* **2015**, *7*, 25227–25236.
(18) Birowosuto, M. D.; Cortecchia, D.; Drozdowski, W.; Brylew, K.; Lachmanski, W.; Bruno, A.; Soci, C. X-ray Scintillation in Lead Halide Perovskite Crystals. *Sci. Rep.* **2016**, *6*, 37254.
(19) Stranks, S. D.; Snaith, H. J. Metal-Halide Perovskites for Photovoltaic and Light-Emitting Devices. *Nat. Nanotechnol.* **2015**, *10*, 391–402.
(20) Kim, Y.-H.; Cho, H.; Heo, J. H.; Kim, T.-S.; Myoung, N.; Lee, C.-L.; Im, S. H.; Lee, T.-W. Multicolored Organic/Inorganic Hybrid Perovskite Light-Emitting Diodes. *Adv. Mater.* **2015**, *27*, 1248–1254.
(21) Kagan, C. R.; Mitzi, D. B.; Dimitrakopoulos, C. D. Organic-Inorganic Hybrid Materials as Semiconducting Channels in Thin-Film Field-Effect Transistors. *Science* **1999**, *286*, 945–947.
(22) Mitzi, D. B.; Dimitrakopoulos, C. D.; Kosbar, L. L. Structurally Tailored Organic–Inorganic Perovskites: Optical Properties and Solution-Processed Channel Materials for Thin-Film Transistors. *Chem. Mater.* **2001**, *13*, 3728–3740.
(23) Mitzi, D. B.; Dimitrakopoulos, C. D.; Rosner, J.; Medeiros, D. R.; Xu, Z.; Noyan, C. Hybrid Field-Effect Transistor Based on a Low-Temperature Melt-Processed Channel Layer. *Adv. Mater.* **2002**, *14*, 1772–1776.
(24) Li, F.; Ma, C.; Wang, H.; Hu, W.; Yu, W.; Sheikh, A. D.; Wu, T. Ambipolar Solution-Processed Hybrid Perovskite Phototransistors. *Nat. Commun.* **2015**, *6*, 8238.
(25) Matsushima, T.; Hwang, S.; Sandanayaka, A. S. D.; Qin, C.; Terakawa, S.; Fujihara, T.; Yahiro, M.; Adachi, C. Solution-Processed Organic-Inorganic Perovskite Field-Effect Transistors with High Hole Mobilities. *Adv. Mater.* **2016**, *28*, 10275–10281.
(26) Senanayak, S. P.; Yang, B.; Thomas, T. H.; Giesbrecht, N.; Huang, W.; Gann, E.; Nair, B.; Goedel, K.; Guha, S.; Moya, X.; McNeill, C. R.; Docampo, P.; Sadhanala, A.; Friend, R. H.; Sirringhaus, H. Understanding Charge Transport in Lead Iodide Perovskite Thin-Film Field-Effect Transistors. *Sci. Adv.* **2017**, *3*, No. e1601935.
(27) Yusoff, A. R. b. M.; Kim, H. P.; Li, X.; Kim, J.; Jang, J.; Nazeeruddin, M. K. Ambipolar Triple Cation Perovskite Field Effect Transistors and Inverters. *Adv. Mater.* **2017**, *29*, 1602940.
(28) Liu, X.; Yu, D.; Huo, C.; Song, X.; Gao, Y.; Zhang, S.; Zeng, H. A Perovskite Light-Emitting Device Driven by Low-Frequency Alternating Current Voltage. *Adv. Opt. Mater.* **2018**, *6*, 1800206.
(29) Capelli, R.; Toffanin, S.; Generali, G.; Usta, H.; Facchetti, A.; Muccini, M. Organic Light-Emitting Transistors with an Efficiency that Outperforms the Equivalent Light-Emitting Diodes. *Nat. Mater.* **2010**, *9*, 496–503.
(30) McCarthy, M. A.; Liu, B.; Donoghue, E. P.; Kravchenko, I.; Kim, D. Y.; So, F.; Rinzler, A. G. Low-Voltage, Low-Power, Organic Light-Emitting Transistors for Active Matrix Displays. *Science* **2011**, *332*, 570–573.
(31) Eames, C.; Frost, J. M.; Barnes, P. R. F.; O'Regan, B. C.; Walsh, A.; Islam, M. S. Ionic Transport in Hybrid Lead Iodide Perovskite Solar Cells. *Nat. Commun.* **2015**, *6*, 7497.
(32) De Bastiani, M.; Dell'Erba, G.; Gandini, M.; D'Innocenzo, V.; Neutzner, S.; Kandada, A. R. S.; Grancini, G.; Binda, M.; Prato, M.; Ball, J. M.; Caironi, M.; Petrozza, A. Ion Migration and the Role of Preconditioning Cycles in the Stabilization of the J–V Characteristics of Inverted Hybrid Perovskite Solar Cells. *Adv. Energy Mater.* **2016**, *6*, 1501453.
(33) Filippetti, A.; Delugas, P.; Saba, M. I.; Mattoni, A. Entropy-Suppressed Ferroelectricity in Hybrid Lead-Iodide Perovskites. *J. Phys. Chem. Lett.* **2015**, *6*, 4909–4915.
(34) Hoque, M. N. F.; Yang, M.; Li, Z.; Islam, N.; Pan, X.; Zhu, K.; Fan, Z. Polarization and Dielectric Study of Methylammonium Lead Iodide Thin Film to Reveal its Nonferroelectric Nature under Solar Cell Operating Conditions. *ACS Energy Lett.* **2016**, *1*, 142–149.
(35) Mattoni, A.; Filippetti, A.; Saba, M. I.; Delugas, P. Methylammonium Rotational Dynamics in Lead Halide Perovskite by Classical Molecular Dynamics: The Role of Temperature. *J. Phys. Chem. C* **2015**, *119*, 17421–17428.
(36) Fabini, D. H.; Hogan, T.; Evans, H. A.; Stoumpos, C. C.; Kanatzidis, M. G.; Seshadri, R. Dielectric and Thermodynamic Signatures of Low-Temperature Glassy Dynamics in the Hybrid Perovskites CH3NH3PbI3 and HC(NH2)2PbI3. *J. Phys. Chem. Lett.* **2016**, *7*, 376–381.
(37) Labram, J. G.; Fabini, D. H.; Perry, E. E.; Lehner, A. J.; Wang, H.; Glaudell, A. M.; Wu, G.; Evans, H.; Buck, D.; Cotta, R.; Echegoyen, L.; Wudl, F.; Seshadri, R.; Chabinyc, M. L. Temperature-Dependent Polarization in Field-Effect Transport and Photovoltaic Measurements of Methylammonium Lead Iodide. *J. Phys. Chem. Lett.* **2015**, *6*, 3565–3571.
(38) Azpiroz, J. M.; Mosconi, E.; Bisquert, J.; De Angelis, F. Defect Migration in Methylammonium Lead Iodide and its Role in Perovskite Solar Cell Operation. *Energy Environ. Sci.* **2015**, *8*, 2118–2127.
(39) Snaith, H. J.; Abate, A.; Ball, J. M.; Eperon, G. E.; Leijtens, T.; Noel, N. K.; Stranks, S. D.; Wang, J. T.-W.; Wojciechowski, K.; Zhang, W. Anomalous Hysteresis in Perovskite Solar Cells. *J. Phys. Chem. Lett.* **2014**, *5*, 1511–1515.
(40) Unger, E. L.; Hoke, E. T.; Bailie, C. D.; Nguyen, W. H.; Bowring, A. R.; Heumüller, T.; Christoforo, M. G.; McGehee, M. D. Hysteresis and Transient Behavior in Current-Voltage Measurements

DOI: 10.1021/acsami.8b11057
ACS Appl. Mater. Interfaces 2018, 10, 37316–37325

of Hybrid-Perovskite Absorber Solar Cells. *Energy Environ. Sci.* **2014**, *7*, 3690−3698.
(41) Bruno, A.; Cortecchia, D.; Chin, X. Y.; Fu, K.; Boix, P. P.; Mhaisalkar, S.; Soci, C. Temperature and Electrical Poling Effects on Ionic Motion in MAPbI3 Photovoltaic Cells. *Adv. Energy Mater.* **2017**, *7*, 1700265.
(42) Yang, X.; Zhang, X.; Deng, J.; Chu, Z.; Jiang, Q.; Meng, J.; Wang, P.; Zhang, L.; Yin, Z.; You, J. Efficient Green Light-Emitting Diodes Based on Quasi-Two-Dimensional Composition and Phase Engineered Perovskite with Surface Passivation. *Nat. Commun.* **2018**, *9*, 570.
(43) Tsai, H.; Nie, W.; Blancon, J.-C.; Stoumpos, C. C.; Soe, C. M. M.; Yoo, J.; Crochet, J.; Tretiak, S.; Even, J.; Sadhanala, A.; Azzellino, G.; Brenes, R.; Ajayan, P. M.; Bulović, V.; Stranks, S. D.; Friend, R. H.; Kanatzidis, M. G.; Mohite, A. D. Stable Light-Emitting Diodes Using Phase-Pure Ruddlesden-Popper Layered Perovskites. *Adv. Mater.* **2018**, *30*, 1704217.
(44) Brenner, T. M.; Egger, D. A.; Rappe, A. M.; Kronik, L.; Hodes, G.; Cahen, D. Are Mobilities in Hybrid Organic-Inorganic Halide Perovskites Actually "High"? *J. Phys. Chem. Lett.* **2015**, *6*, 4754−4757.
(45) Jovicic, A.; Li, J.; Richardson, T. Visible Light Communication: Opportunities, Challenges and the Path to Market. *IEEE Commun. Mag.* **2013**, *51*, 26−32.
(46) Tze, S. M.; Ng, K. K. *Physics of Semiconductor Devices*, 3rd ed.; John Wiley & Sons, Inc.: Hoboken, NJ, 2007.
(47) Kumawat, N. K.; Jain, N.; Dey, A.; Narasimhan, K. L.; Kabra, D. Quantitative Correlation of Perovskite Film Morphology to Light Emitting Diodes Efficiency Parameters. *Adv. Funct. Mater.* **2017**, *27*, 1603219.
(48) Jeon, N. J.; Noh, J. H.; Kim, Y. C.; Yang, W. S.; Ryu, S.; Seok, S. I. Solvent engineering for high-performance inorganic-organic hybrid perovskite solar cells. *Nat. Mater.* **2014**, *13*, 897−903.
(49) Swensen, J. S.; Soci, C.; Heeger, A. J. Light Emission from an Ambipolar Semiconducting Polymer Field-Effect Transistor. *Appl. Phys. Lett.* **2005**, *87*, 253511.
(50) Zhang, C.; Chen, P.; Hu, W. Organic Light-Emitting Transistors: Materials, Device Configurations, and Operations. *Small* **2016**, *12*, 1252−1294.
(51) Wu, X.; Trinh, M. T.; Niesner, D.; Zhu, H.; Norman, Z.; Owen, J. S.; Yaffe, O.; Kudisch, B. J.; Zhu, X.-Y. Trap States in Lead Iodide Perovskites. *J. Am. Chem. Soc.* **2015**, *137*, 2089−2096.
(52) Baumann, A.; Tvingstedt, K.; Heiber, M. C.; Väth, S.; Momblona, C.; Bolink, H. J.; Dyakonov, V. Persistent Photovoltage in Methylammonium Lead Iodide Perovskite Solar Cells. *APL Mater.* **2014**, *2*, 081501.
(53) Necliudov, P. V.; Shur, M. S.; Gundlach, D. J.; Jackson, T. N. Contact Resistance Extraction in Pentacene Thin Film Transistors. *Solid-State Electron.* **2003**, *47*, 259−262.
(54) Leguy, A. M. A.; Frost, J. M.; McMahon, A. P.; Sakai, V. G.; Kockelmann, W.; Law, C.; Li, X.; Foglia, F.; Walsh, A.; O'Regan, B. C.; Nelson, J.; Cabral, J. T.; Barnes, P. R. F. The Dynamics of Methylammonium Ions in Hybrid Organic−Inorganic Perovskite Solar Cells. *Nat. Commun.* **2015**, *6*, 7124.
(55) Kjelstrup-Hansen, J.; Liu, X.; Henrichsen, H. H.; Thilsing-Hansen, K.; Rubahn, H.-G. Conduction and Electroluminescence from Organic Continuous and Nanofiber Thin Films. *Phys. Status Solidi C* **2010**, *7*, 2763−2766.
(56) Liu, X.; Wallmann, I.; Boudinov, H.; Kjelstrup-Hansen, J.; Schiek, M.; Lützen, A.; Rubahn, H.-G. AC-Biased Organic Light-Emitting Field-Effect Transistors from Naphthyl End-Capped Oligothiophenes. *Org. Electron.* **2010**, *11*, 1096−1102.
(57) Sung, J.; Choi, Y. S.; Kang, S. J.; Cho, S. H.; Lee, T.-W.; Park, C. AC Field-Induced Polymer Electroluminescence with Single Wall Carbon Nanotubes. *Nano Lett.* **2011**, *11*, 966−972.
(58) Zaki, T.; Rödel, R.; Letzkus, F.; Richter, H.; Zschieschang, U.; Klauk, H.; Burghartz, J. N. AC Characterization of Organic Thin-Film Transistors with Asymmetric Gate-to-Source and Gate-to-Drain Overlaps. *Org. Electron.* **2013**, *14*, 1318−1322.
(59) Yamao, T.; Shimizu, Y.; Terasaki, K.; Hotta, S. Organic Light-Emitting Field-Effect Transistors Operated by Alternating-Current Gate Voltages. *Adv. Mater.* **2008**, *20*, 4109−4112.
(60) Ohtsuka, Y.; Ishizumi, A.; Yanagi, H. Light-emitting field-effect transistors with π-conjugated liquid crystalline polymer driven by AC-gate voltages. *Org. Electron.* **2012**, *13*, 1710−1715.
(61) Ohshima, Y.; Kohn, H.; Manaka, T.; Iwamoto, M. Space Charge Field Effect on Light Emitting from Tetracene Field-Effect Transistor Under AC Electric Field. *Thin Solid Films* **2009**, *518*, 583−587.
(62) Hotta, S. Optically and Electrically Excited Emissions from Organic Semiconducting Oligomer Crystals. *Polym. Int.* **2017**, *66*, 223−236.
(63) Liu, X.; Kjelstrup-Hansen, J.; Boudinov, H.; Rubahn, H.-G. Charge-Carrier Injection Assisted by Space-Charge Field in AC-driven Organic Light-Emitting Transistors. *Org. Electron.* **2011**, *12*, 1724−1730.
(64) Chen, Y.; Xia, Y.; Smith, G. M.; Carroll, D. L. Frequency-Dependent, Alternating Current-Driven, Field-Induced Polymer Electroluminescent Devices with High Power Efficiency. *Adv. Mater.* **2014**, *26*, 8133−8140.
(65) Cho, S. H.; Sung, J.; Hwang, I.; Kim, R. H.; Choi, Y. S.; Jo, S. S.; Lee, T. W.; Park, C. High Performance AC Electroluminescence from Colloidal Quantum Dot Hybrids. *Adv. Mater.* **2012**, *24*, 4540−4546.
(66) Chen, Y.; Xia, Y.; Sun, H.; Smith, G. M.; Yang, D.; Ma, D.; Carroll, D. L. Solution-Processed Highly Efficient Alternating Current-Driven Field-Induced Polymer Electroluminescent Devices Employing High-kRelaxor Ferroelectric Polymer Dielectric. *Adv. Funct. Mater.* **2014**, *24*, 1501−1508.
(67) Ohshima, Y.; Kohn, H.; Lim, E.; Manaka, T.; Iwamoto, M. Observation of Carrier Behavior in Organic Field-Effect Transistors with Electroluminescence under. *Jpn. J. Appl. Phys.* **2008**, *47*, 3200.
(68) Maddalena, F.; de Falco, C.; Caironi, M.; Natali, D. Assessing the Width of Gaussian Density of States in Organic Semiconductors. *Org. Electron.* **2015**, *17*, 304−318.
(69) Stroppa, A.; Quarti, C.; De Angelis, F.; Picozzi, S. Ferroelectric Polarization of CH3NH3PbI3: A Detailed Study Based on Density Functional Theory and Symmetry Mode Analysis. *J. Phys. Chem. Lett.* **2015**, *6*, 2223−2231.
(70) Röhm, H.; Leonhard, T.; Hoffmann, M. J.; Colsmann, A. Ferroelectric Domains in Methylammonium Lead Iodide Perovskite Thin-Films. *Energy Environ. Sci.* **2017**, *10*, 950−955.
(71) Stroppa, A.; Di Sante, D.; Barone, P.; Bokdam, M.; Kresse, G.; Franchini, C.; Whangbo, M.-H.; Picozzi, S. Tunable Ferroelectric Polarization and its Interplay with Spin−Orbit Coupling in Tin Iodide Perovskites. *Nat. Commun.* **2014**, *5*, 5900.
(72) Ortiz, R. P.; Facchetti, A.; Marks, T. J. High-kOrganic, Inorganic, and Hybrid Dielectrics for Low-Voltage Organic Field-Effect Transistors. *Chem. Rev.* **2010**, *110*, 205−239.
(73) Gwinner, M. C.; Kabra, D.; Roberts, M.; Brenner, T. J. K.; Wallikewitz, B. H.; McNeill, C. R.; Friend, R. H.; Sirringhaus, H. Highly Efficient Single-Layer Polymer Ambipolar Light-Emitting Field-Effect Transistors. *Adv. Mater.* **2012**, *24*, 2728−2734.

DOI: 10.1021/acsami.8b11057
ACS Appl. Mater. Interfaces 2018, 10, 37316−37325